Chapter 1

Introduction

This thesis involves the development and application of adjoint methods to the seismic tomographic inverse problem. The success of an inverse problem depends primarily on the quality and coverage of the data, and on the accuracy of the forward modeling tool within the inverse problem. Our forward modeling tool is the spectral-element method (SEM), which has been developed for regional and global scales of seismic wave propagation (*Komatitsch and Vilotte*, 1998; *Komatitsch and Tromp*, 2002a,b; *Komatitsch et al.*, 2004).

The remaining chapters emphasize the inverse problem, so we will briefly state the essential equations of the forward problem of seismic wave propagation. The equation of motion for an anelastic Earth is given by

$$\rho \frac{\partial^2 \mathbf{s}}{\partial t^2} = \boldsymbol{\nabla} \cdot \mathbf{T} + \mathbf{f}, \tag{1.1}$$

where $\rho(\mathbf{x})$ denotes the density distribution, $\mathbf{s}(\mathbf{x},t)$ the seismic wavefield, $\mathbf{T}(\mathbf{x},t)$ the stress tensor, and $\mathbf{f}(\mathbf{x},t)$ the earthquake source. (We neglect rotation and self-gravitation.)

If the medium is elastic, then we apply Hooke's law

$$\mathbf{T} = \mathbf{c} : \boldsymbol{\nabla}\mathbf{s} \,, \tag{1.2}$$

which states that the stress is linearly related to the displacement gradient $\boldsymbol{\nabla}\mathbf{s}$ (strain) through the fourth-order elastic tensor $\mathbf{c}(\mathbf{x})$.

If the elastic medium is isotropic, then the elements of $\mathbf{c}$ are described by two parameters:

$$c_{jklm} = (\kappa - \tfrac{2}{3}\mu)\delta_{jk}\delta_{lm} + \mu(\delta_{jl}\delta_{km} + \delta_{jm}\delta_{kl}), \tag{1.3}$$

where $\mu(\mathbf{x})$ is the shear modulus and $\kappa(\mathbf{x})$ is the bulk modulus.

In general, the `SPECFEM3D` software (*Komatitsch and Tromp*, 2002a; *Komatitsch et al.*, 2004) takes into account the full complexity of seismic wave propagation, including attenuation, full anisotropy, topography, and ocean loads, as well as asymmetries relevant for very long-period waves, such as Earth's ellipticity and self-gravitation. In this thesis, the SEM (2D and 3D version) has been used primarily for elastic, isotropic Earth models. Attenuation is only implemented within the sedimentary basins in the Los Angeles region for 3D wavefield simulations.

1.1 The inverse problem (and thesis overview)

The forward modeling tool within our tomographic inverse problem is the SEM, either in a 2D wave propagation code (*Tromp et al.*, 2005; *Tape et al.*, 2007) or a 3D version (*Komatitsch et al.*, 2004). The challenge for tomographers is how to harness the accuracy of these forward-modeling methods for the inverse problem. One approach is to utilize so-called adjoint methods (*Tarantola*, 1984; *Talagrand and Courtier*, 1987; *Courtier and Talagrand*, 1987), which are related to concepts developed in seismic imaging (*Claerbout*, 1971; *McMechan*, 1982). *Tromp et al.* (2005) demonstrated the theoretical connections between adjoint methods, seismic tomography, time reversal imaging (e.g., *Fink*, 1997), and finite-frequency "banana-doughnut" kernels (e.g., *Dahlen et al.*, 2000).

Chapter 2 (*Tape et al.*, 2007) extends the study of *Tromp et al.* (2005) in the direction of an iterative inverse problem based on adjoint methods. The 2D synthetic inversion experiments are performed using three different approaches: (1) a gradient-based fully numerical approach using adjoint methods — we call this "adjoint tomography"; (2) a classical approach using finite-frequency kernels; and (3) a classical approach using rays. By "classical," we mean that a model is expanded into basis functions, and the sensitivity of each measurement is described using rays or kernels derived from a simple (homogeneous or 1D) reference model (e.g., Table A.1).

Chapter 3 contains excerpts from *Tromp et al.* (2005) that demonstrate the ability of the adjoint approach to isolate the volumetric region that a seismic waveform “sees” as it propagates through a (1D or 3D) reference model. We implemented adjoint methods within a 2D SEM code, and then designed and conducted series of numerical experiments. (For a quick visual understanding of how finite-frequency kernels are formed via the interaction between the forward wavefield and the adjoint wavefield, one should begin with Chapter 3.)

The frequency dependence of the seismic wavefield plays a critical role in the forward and inverse problems, and we illustrate some basic features in Figures 1.1 and 1.2. A seismic waveform containing longer-period energy will sample (or “see”) a broader region along the path between the source and station (Figure 1.1). Thus, by making measurements over multiple frequency bands, we should be able to better sample the model, and to make changes that are required by the data. With the implementation of adjoint methods within a 3D SEM code (*Liu and Tromp*, 2006), it became possible to visualize finite-frequency kernels that could be complicated, even for simple 1D layers models (Figure 1.2). These adjoint capabilities within the 3D SEM code provided the possibility for a full inverse problem using actual data (Chapter 6).

Chapter 4 presents an approach to compute an optimal model update for a given iteration within the inverse problem. The approach relies on subspace projection techniques (*Kennett et al.*, 1988; *Sambridge et al.*, 1991), and it does not require any additional forward or adjoint wavefield simulations.

In preparation for a tomographic inversion that begins with an initial 3D reference model, *Maggi et al.* (2009) developed an automated algorithm for picking measurement time windows containing recorded and synthetic waveforms. Chapter 5 contains excerpts from *Maggi et al.* (2009), emphasizing examples for southern California.

Chapter 6 presents an application of adjoint tomography to southern California. A preview of this study is exemplified in Figures 1.3–1.5. Figure 1.3 demonstrates the highly variable frequency content within a three-component seismogram. It also shows the appearance of the wavefield over different period ranges.

This thesis marks the beginning of an endeavor into seismic tomography using adjoint methods. Future work will undoubtedly refine the current procedures and include additional complexity. First, we will implement — or possibly invert for — attenuation in southern California in regions of tomographically documented sedimentary basins.[1] Sec-

---

[1] Attenuation is already implemented in the basins of *Komatitsch et al.* (2004) and *Lovely et al.* (2006)

ond, we will consider crustal anisotropy (e.g., *Christensen and Mooney*, 1995; *Paulssen*, 2004) and boundary surfaces (e.g., *Fuis et al.*, 2003; *Yan and Clayton*, 2007; *Bleibinhaus et al.*, 2007) as inversion parameters. The prospects of inverting for these parameters are discussed in *Sieminski et al.* (2007) for anisotropy and in *Dahlen* (2005) and *Tromp et al.* (2005) for boundary surfaces.

Finally, we will apply seismic reflection imaging techniques (e.g., *Kiyashchenko et al.*, 2007) to identify and quantify lateral and vertical reflectors in southern California. Figure 1.6 shows an example of a Rayleigh-wave reflection off of the Tehachapi Mountains. The reflected waveform is not apparent in the synthetic seismogram from the initial 3D model ($\mathbf{m}_{00}$) but is in the final model ($\mathbf{m}_{16}$). The ability to capture such waveforms on individual seismograms demonstrates the possibility of enhancing tomographic coverage by delving deeper into seismograms while using the same set of earthquakes and stations.

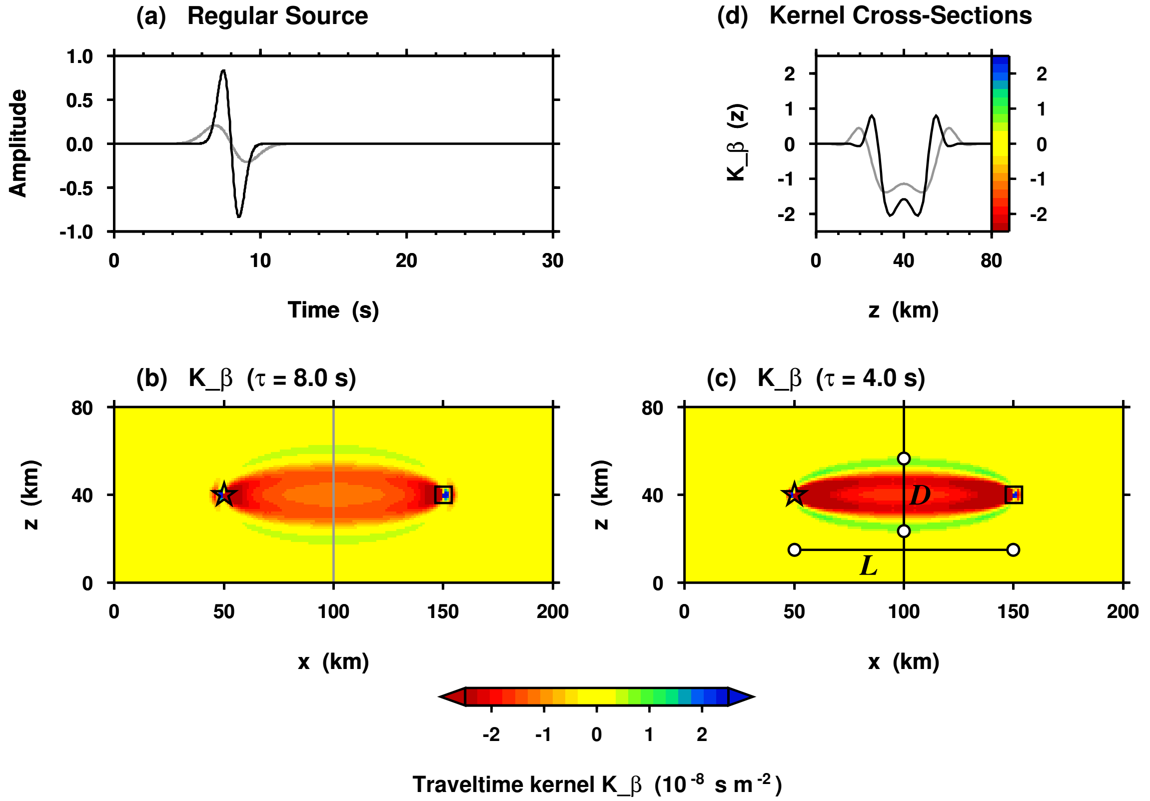

Figure 1.1: Frequency dependence of sensitivity kernels (after *Tromp et al.*, 2005, Figure 6). (a) Two source-time functions for the regular wavefield with durations of $\tau = 8.0$ s (gray) and $\tau = 4.0$ s (black) (see Eq. 3.2). (b) $\bar{K}_{\beta(\alpha\rho)}$ for $\tau = 8.0$ s. (c) $\bar{K}_{\beta(\alpha\rho)}$ for $\tau = 4.0$ s. $D = 33$ km is the width of the first Fresnel zone, estimated as $D \approx \sqrt{\lambda L} = \sqrt{\beta T L}$, where $T = 3.4$ s is the dominant period of the seismic wave, and $\beta = 3.2$ km/s is the shear wavespeed and $L = 100$ km is the path length. (d) Depth cross sections of (b) and (c) at a horizontal distance of $x = 100$ km. As expected, the higher-frequency kernel is narrower in width and greater in amplitude. See Chapter 3 for details on how these kernels were constructed.

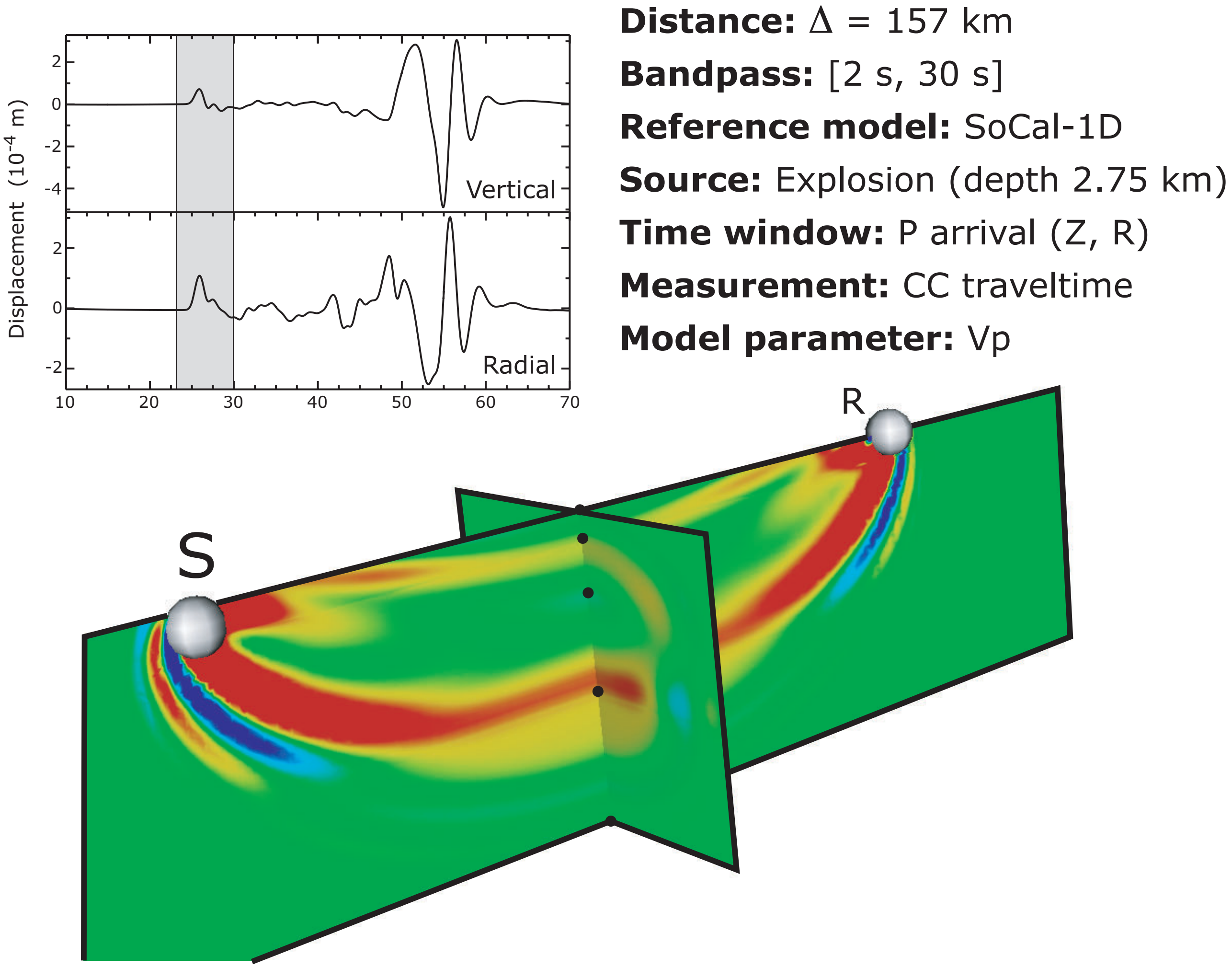

Figure 1.2: Sensitivity kernel for a crustal P wave in a 1D southern California model (*Kanamori and Hadley*, 1975; *Wald et al.*, 1995). The time window highlighted in the vertical and radial components of the seismograms corresponds to the volumetric sensitivity kernel, shown in two perpendicular cross sections. S is the source location, and R is the receiver. The dots mark the layer boundaries of the 1D model at 5.5, 16.0, and 32.0 km, with the bottom at 60.0 km. This sensitivity kernel indicates that the P arrival is a combination of Pn, diffracted along the Moho, and PmP, reflected at the Moho. Several factors, listed in the upper right, influence the nature of the sensitivity kernel, which can be interpreted as follows: "Given a cross-correlation traveltime measurement, ΔT, between observed and simulated seismic waveforms (bandpass period range 2–30 s) within the selected time window, the sensitivity kernel illuminates the volumetric region of the V_{P} wavespeed model that should be perturbed in order to reduce ΔT." (However, this does not ensure that the wavespeed perturbation is a step in the direction of the actual wavespeed structure, because the ΔT could have arisen from an incorrect description of the earthquake source.)

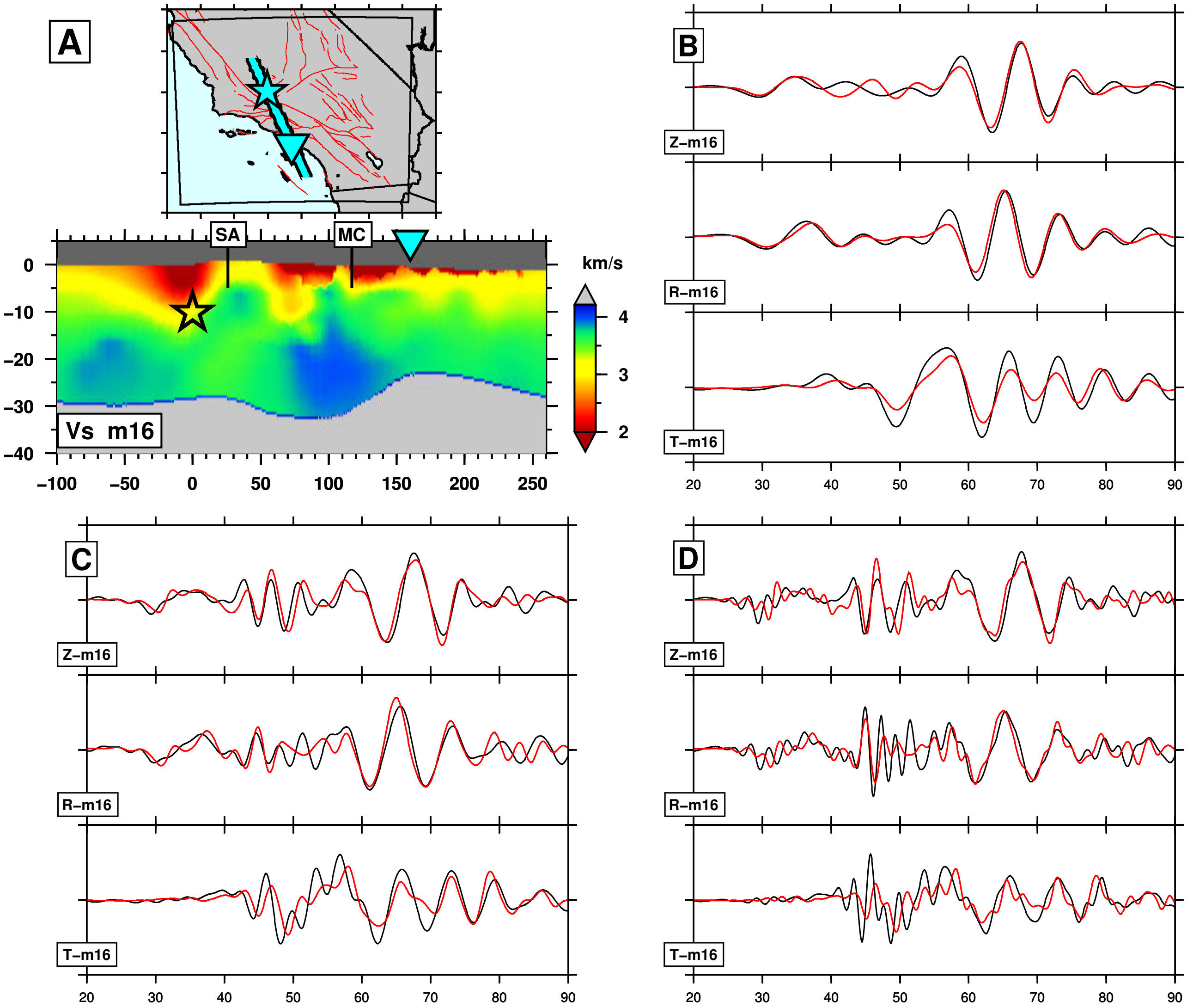

Figure 1.3: The frequency dependence of the seismic wavefield. (a) Cross section of adjoint tomography crustal model $\mathbf{m}_{16}$ (Chapter 6) from event 14186612 to station FMP.CI. SA, San Andreas fault; MC, Malibu Coast fault. (b) Data (black) and 3D synthetics (red), filtered in the period range 6–30 s. Z, vertical component, R, radial component, T, transverse component. (c) Same as (b), for the period range 3–30 s. (d) Same as (b), for the period range 2–30 s.

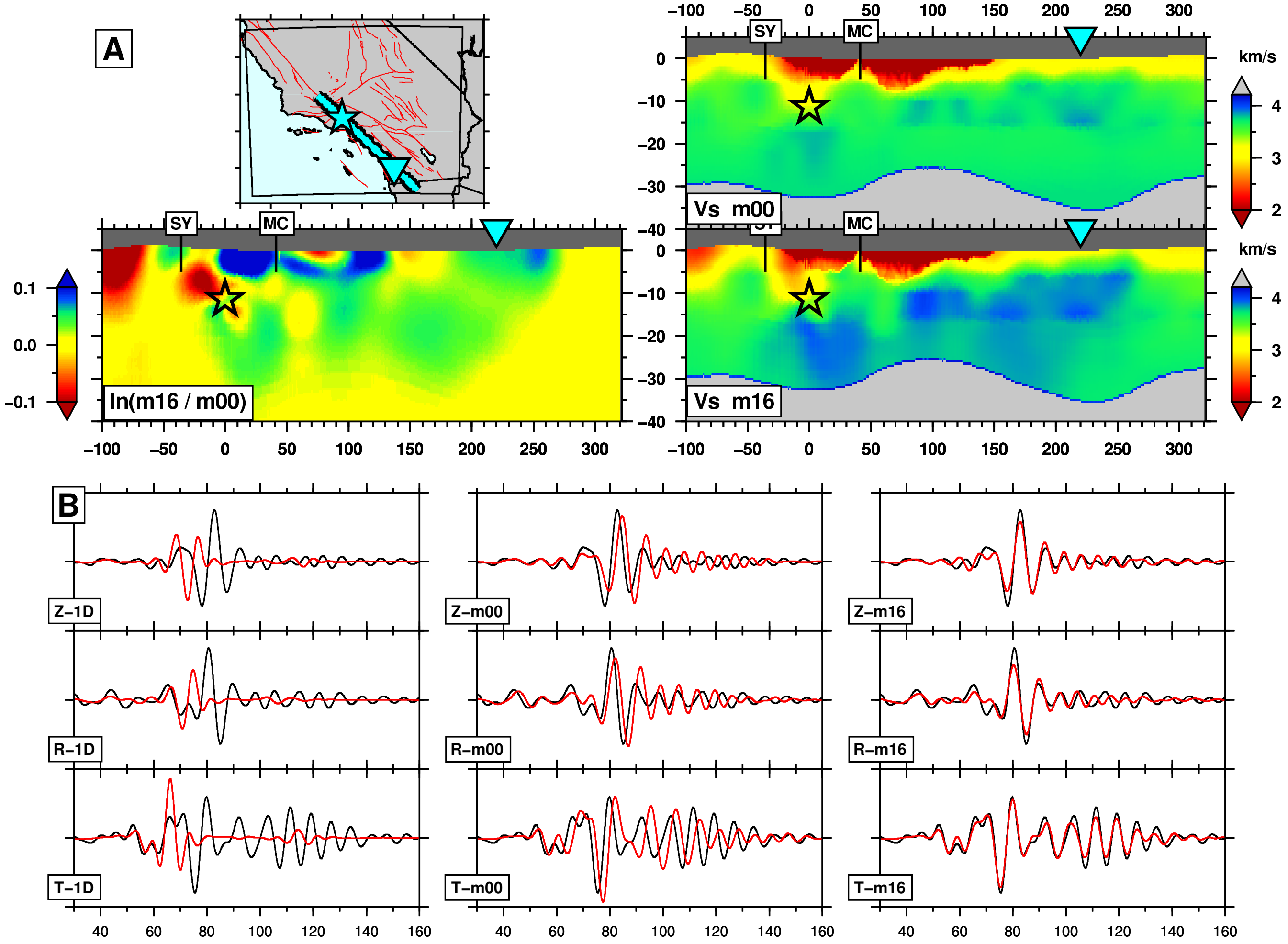

Figure 1.4: Iterative improvement in seismic waveforms. (a) Initial 3D model $\mathbf{m}_{00}$, final 3D model $\mathbf{m}_{16}$, and the difference between the two models, $\ln(\mathbf{m}_{16}/\mathbf{m}_{00})$. (b) Data (black) and 3D synthetics (red), filtered in the period range 6–30 s. Z, vertical component, R, radial component, T, transverse component. Left column: synthetics generated using the standard 1D southern California model (*Kanamori and Hadley*, 1975; *Wald et al.*, 1995). Center column: synthetics generated using $\mathbf{m}_{00}$, the 3D model of *Komatitsch et al.* (2004). Right column: synthetics generated using $\mathbf{m}_{16}$, the 16th iteration of the crustal model.

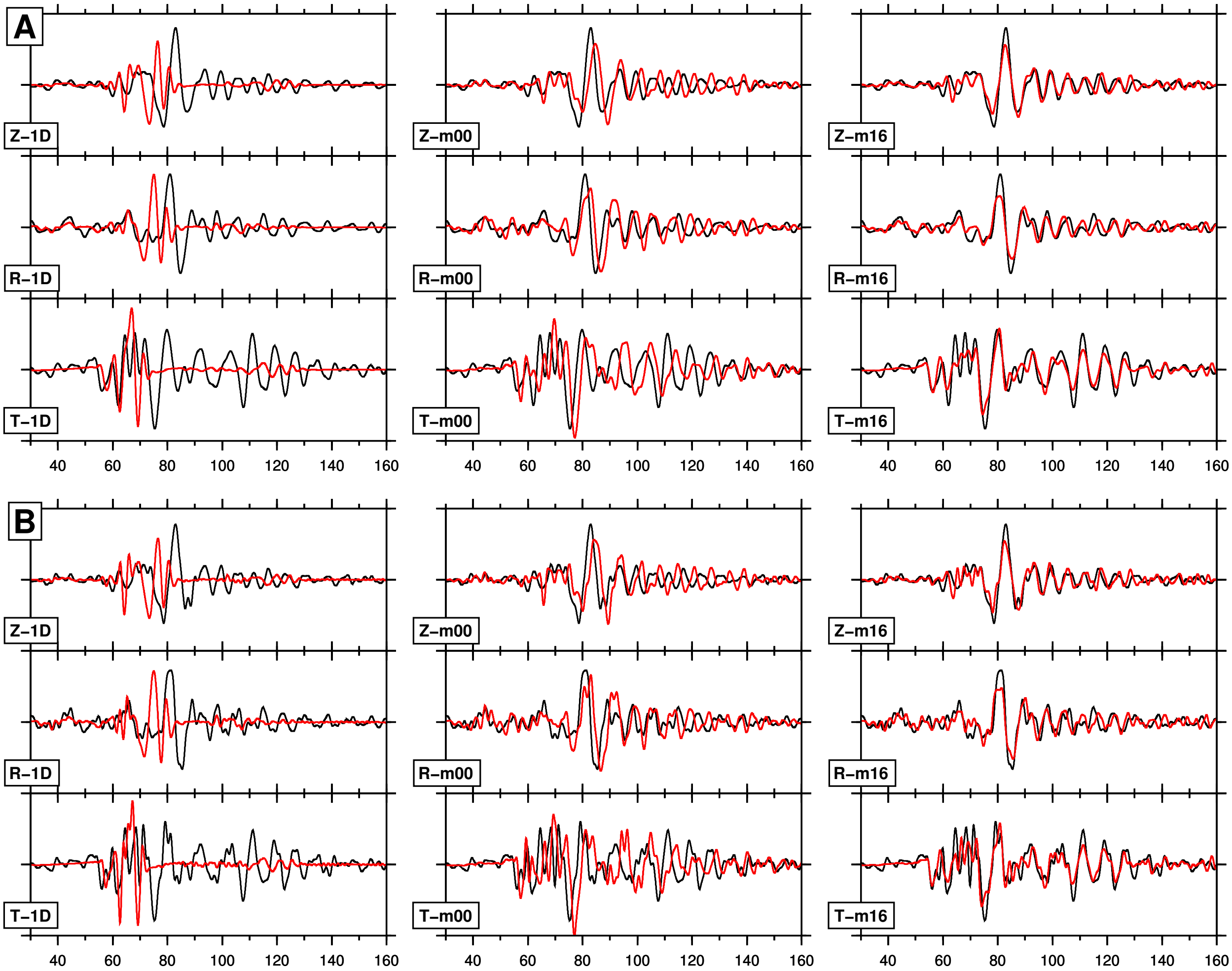

Figure 1.5: Same seismograms as in Figure 1.4b, but for the period ranges 3–30 s (a) and 2–30 s. Z, vertical component, R, radial component, T, transverse component. Left column: synthetics generated using the standard 1D southern California model (*Kanamori and Hadley*, 1975; *Wald et al.*, 1995). Center column: synthetics generated using $\mathbf{m}_{00}$, the 3D model of *Komatitsch et al.* (2004). Right column: synthetics generated using $\mathbf{m}_{16}$, the 16th iteration of the crustal model.

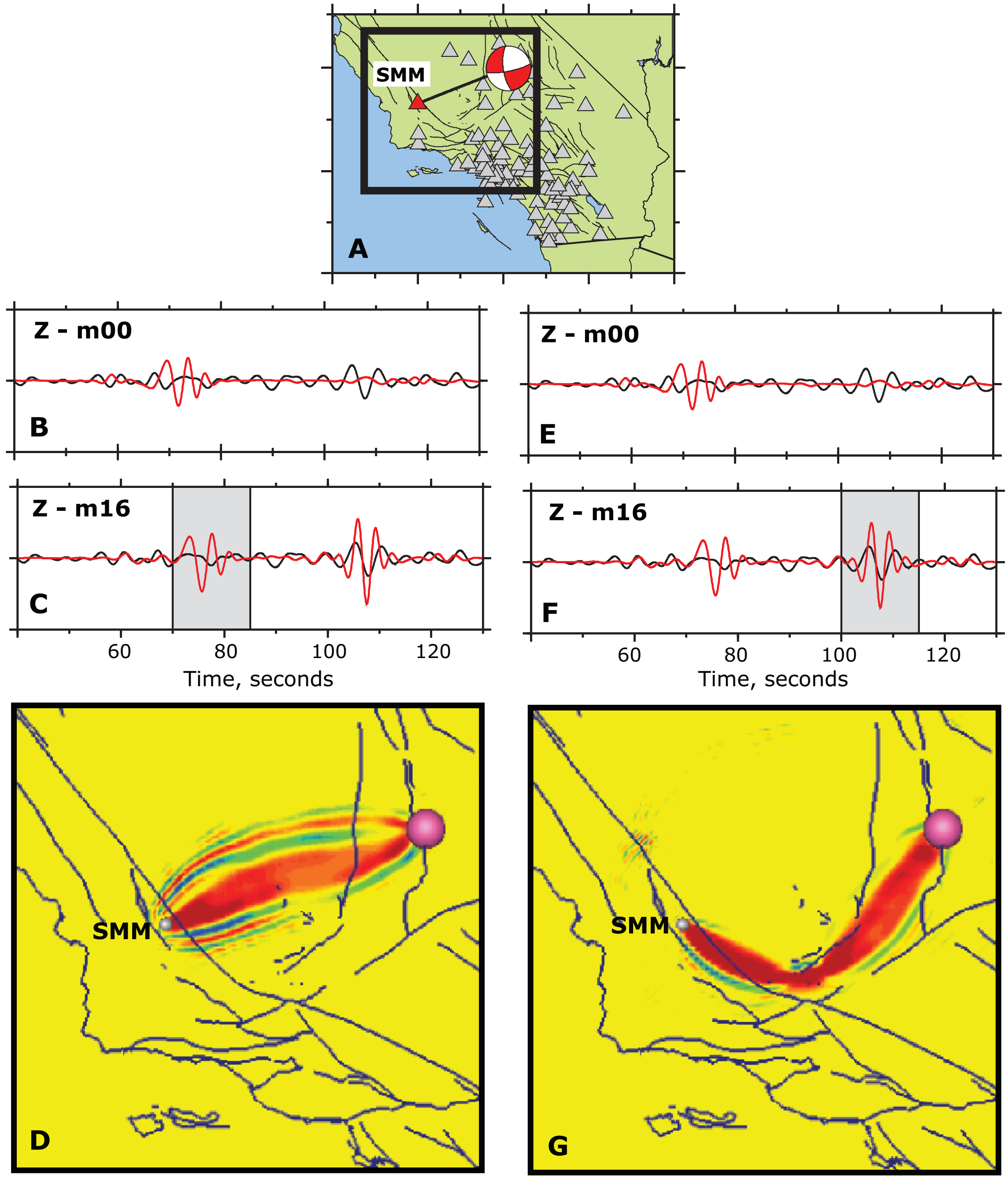

Figure 1.6: Reflected Rayleigh wave at the Tehachapi Mountains. The manually-picked measurement windows shown in (c) and (f) highlight two different surface waves. All seismograms are filtered in the period range 3–30 s. (a) Map showing earthquake source (10992159) and station coverage. Black box shows the region in (d) and (g). (b) Data (black) and $\mathbf{m}_{00}$ 3D synthetics (red). (c) Data (black) and $\mathbf{m}_{16}$ 3D synthetics (red). Synthetic waveform within the time window follows the propagation path shown in (d). The phase of the synthetic waveform is about right ($\Delta T = 1.7$ s), but the amplitude is much to large $\Delta \ln A = -1.5$. (d) Horizontal cross section at 4 km depth of a volumetric sensitivity kernel corresponding to the windowed synthetic waveform in (c). The path illuminates the "direct" Rayleigh wave, though the path does not lie on the great circle between source and station. (e)–(g) Same as (b)–(d), but highlighting the second time window, which is only apparent in the $\mathbf{m}_{16}$ synthetics. The Rayleigh wave reflects at the Tehachapi Mountains, near the southernmost San Joaquin basin, before reaching SMM.